Battery Pack Shape Optimization using Transient Heat Conduction Coupled with Cell-Discharge Analysis

Mark K. Leader*
NASA Glenn Research Center, Cleveland, OH 44135

Battery electric systems exhibit significant time-dependence, especially when evaluated in the context of an aircraft mission profile with continually changing power demands. Additionally, when evaluating battery-powered aircraft concepts, it is important to accurately compute the temperature of the batteries and properly characterize the thermal response of the system. The temperature of the batteries has a significant impact on cell performance, in addition to safety considerations of maintaining battery temperatures below their operating limit. Because of these considerations, battery models for preliminary design and optimization of aircraft should include the capability to accurately compute the temperature distribution within the battery pack. Furthermore, battery pack designs should be as light-weight as possible to maximize the pack energy density, while also considering battery temperature limits. Here, we demonstrate a simultaneous trajectory and shape optimization of a battery pack concept, using a transient heat transfer finite element model coupled with a time-varying cell-discharge battery model to provide this capability. The transient finite-element analysis is done using TACS, and the cell-discharge battery model uses OpenMDAO and dymos. Including the transient finite element problem in the loop enables accurate temperatures that can be passed back to the cell discharge model, while the cell discharge model can supply the finite element model with time-varying heat boundary conditions, further benefiting the fidelity of the thermal response of the batteries. We first demonstrate the coupling capability between the battery cell-discharge model and the transient finite-element heat transfer through an optimization which computes the optimal current profile for the battery pack while ensuring the battery temperatures remain below their operational limit. We then build on this optimization by adding shape optimization to the problem, which allows us to consider a composite objective function which also minimizes the mass of the battery pack, while also producing an optimal current discharge profile.

*Research Engineer, Propulsion Systems Analysis Branch, AIAA Member. Email: mark.leader@nasa.gov

Nomenclature

Acronyms

c	Material specific heat capacity (J/kg · K)
d_{cell}	Cell diameter (mm)
$f, \mathbf{f}$	Function value, generic
I	Current (A)
$I_{\max}$	Maximum allowable current (A)
m	Mass (kg)
n_{p}	Number of cells in parallel
n_{s}	Number of cells in series
$\mathbf{q}$	Time-varying scalar heat flux (W)
Q	Rate of total heat generated by the battery pack (W)
$\mathbf{Q}$	Right-hand-side in the matrix-form of the transient heat transfer finite element equations (W)
r	Hole radius in the battery pack geometry (mm)
R_0	Ohmic resistance
R_{Thev}	Polarization resistance
s	Relative spacing between battery cells
SOC	State-of-charge (%)
t	Time (s)
T	Temperature (°C)
$\mathbf{T}_{\mathrm{avg}}$	Spatially-averaged time-varying temperature of the battery cells (°C) $\in \mathbb{R}^{n_{\mathrm{TACS}}}$
T_{KS}	Approximate maximum temperature of the battery cells over all time (°C)
$\mathbf{u}$	State-variable vector
U_{oc}	Open-circuit voltage (V)
$\mathbf{x}$	Design variable vector
$\mathbf{X}_{\mathrm{node}}$	Nodal coordinate array
α	Scale factor in composite objective function for shape optimization
Δs	Change in the relative spacing between cells
$\Delta\phi$	Change in the relative hole size
$\boldsymbol{\theta}$	Temperature variable in the continuous form of the heat transfer PDE (°C)
κ	Material thermal conductivity (W/m · K)
ρ	Material density (ks/m^3)
ϕ	Relative hole size; hole radius divided by the maximum allowable radius
$\boldsymbol{\psi}$	Adjoint vector

Subscripts

interp	Values interpolated from the dymos time-discretization to the TACS time-discretization
k	Iteration in time
lb	Lower-bound
ref	Reference value for normalization
slack	Design variables used for coupling between TACS and dymos
Th, Thev	Thevenin-equivalent circut model
ub	Upper-bound

I. Introduction

Battery-electric propulsion will be a significant contributing factor in reducing the environmental impact of aviation, supporting NASA's objectives of reducing net CO_2 emissions to zero by 2050 [1]. Developing new aircraft concepts with battery-electric propulsion presents previously unseen design challenges that are uniquely handled by gradient based optimization frameworks, due to the tight coupling between many subsystems at play. Among these, the interaction between the battery packs and the associated thermal demands is one that we focus on for this work. Modeling the discharge characteristics of the batteries requires their temperature as an input. Additionally, as a safety concern, the battery cell temperatures need to be monitored to ensure that they stay below their operating temperature, or else they will go into thermal runaway. Regulating the thermal loads generated by the batteries, and also mitigating the consequences of a thermal runaway event are some of the most critical challenges in battery pack design for aircraft. But before these challenges can be addressed in the context of an overall aircraft optimization, an accurate characterization of the battery pack thermal response is required. For this work, we will demonstrate an integration of two models to accurately characterize the thermal response of a battery pack system during a combined aircraft and mission optimization. Specifically, we are integrating a battery cell discharge model – to compute the time-varying current, voltage, and other relevant parameters, with a transient finite element heat transfer model – to accurately resolve the temperatures of the battery pack, both spatially within the pack, and at every point in time relevant to the mission. Additionally, battery pack designs should be made as light-weight as possible, while also ensuring that battery temperatures are kept below their operational limit. To do this, we employ shape optimization of the battery pack (using the geometry shown in Fig. 1) which is performed concurrently with the trajectory optimization of the battery pack current.

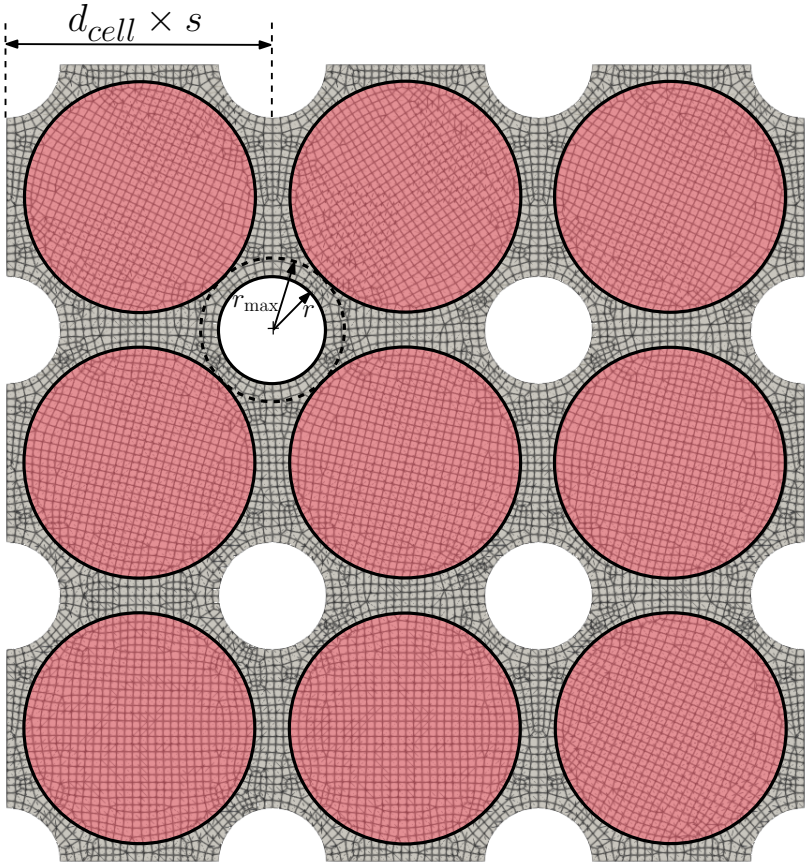

Fig. 1 Battery pack geometry and mesh used for heat transfer finite-element analysis, where the battery cells are highlighted in red and the remaining material is the battery casing material.

II. Methodology

The objective of this work is to combine a transient heat transfer finite element analysis of a battery pack with a cell discharge battery model, and perform a trajectory optimization of that coupled battery model while performing a shape optimization of the battery pack simultaneously. The transient heat transfer finite analysis is solved using TACS* [2, 3], an efficient and open-source finite element tool with analytic gradients using the adjoint method. TACS solves the transient heat transfer problem using time-marching integration schemes, with several algorithm options available. More details are provided in Section II.A.

The battery cell discharge model uses a Thevenin-equivalent circuit model based on Chin et al. [4, 5]. This model is implemented using OpenMDAO† [6] and Dymos‡ [7]. More details about the cell-discharge model are provided in Section II.B. The cell-discharge model has been previously implemented in Aviary, an open-source aircraft and mission optimization too, and demonstrated with a hybrid-electric propulsion model for the TTBW aircraft [8, 9]. The previous work assumed constant cell-temperatures. The cell discharge model is a function of temperature, so assuming a constant temperature will inherently reduce the accuracy of the analysis. Additionally, batteries need to maintain a consistent temperature below their operating limit to ensure safe operation. The work presented in this paper addresses those gaps by adding a time-accurate thermal analysis of the battery temperatures. The finite-element heat transfer model will be coupled with the cell discharge model in both directions: the cell-discharge model computes cell heat output as a function of electric power output during the mission, which gets supplied to the heat transfer model as a time-varying Nuemann boundary condition. The finite element heat transfer model will return time-varying battery temperatures back to the cell-discharge model. Coupling these models will improve the accuracy of both, and also allows us to place a temperature constraint on the batteries during the mission optimization, to ensure safe operation. However, the model coupling is complicated by the fact that both models use different time-integration schemes to converge each model. The transient finite-element heat transfer analysis is integrated in time using a Backwards Difference Formula (BDF) with uniform time-steps. The cell-discharge model is integrated in time using Dymos; in this case, we use the Birkhoff transcription option. The time-integration in Dymos in general will require far fewer points in time than TACS to achieve reliable convergence, and the Dymos time-discretization does not rely on evenly-spaced intervals. The unique time-integration methodologies are justified for the respective models, so there is no reason to try to coerce them to use the same time-discretization just to allow the models to be coupled. Instead, we enforce the coupling by adding additional design variables and constraints to the optimization problem. We will denote the time-dimension of variables as either n_{dymos} or n_{TACS}. We create design variables $\dot{q}_{\text{slack}}$ and T_{slack} both with dimension n_{dymos}. The temperature values T_{slack} are passed as input to the cell-discharge model. The heat-flux slack values are interpolated onto the TACS time-discretization, resulting in a vector of heat flux values $\dot{q}_{\text{TACS}} \in n_{\text{TACS}}$, which are then passed as input to the transient finite-element heat transfer component. The temperatures computed using TACS are interpolated (onto a coarser grid), resulting in $T_{\text{interp}} \in n_{\text{dymos}}$. With this, we add an equality constraint to the optimizer, such that: $T_{\text{slack}} - T_{\text{interp}} = 0$. This leads the optimizer to set the design variable T_{slack} equal to values computed by TACS. Similarly, we add another equality constraint such that: $\dot{q}_{\text{slack}} - \dot{q}_{\text{dymos}} = 0$, which leads the optimizer to set design variables $\dot{q}_{\text{slack}}$ equal to the values computed by the cell-discharge model. The coupling between the transient heat transfer model using TACS, and the cell-discharge model are shown below in the eXtended Design Structure Matrix (XDSM) [10] in Fig. 2.

A. Transient Heat Transfer Finite Element Analysis

The transient heat transfer analysis uses the finite-element method to solve the following equation of motion:

$$\begin{aligned} \rho c \dot{\boldsymbol{\theta}} &= \nabla \cdot (\kappa \nabla \boldsymbol{\theta}), && \text{on } \Omega \text{ for } t \in [0, t_f] \\ \boldsymbol{\theta} &= \tilde{\boldsymbol{\theta}}, && \text{on } \partial_1 \Omega \\ (\kappa \nabla \boldsymbol{\theta}) \cdot \mathbf{n} &= \mathbf{q}, && \text{on } \partial_2 \Omega \\ \boldsymbol{\theta}(t=0) &= \boldsymbol{\theta_0} \end{aligned} \tag{1}$$

where $\boldsymbol{\theta}$ is the temperature state variable in the finite element domain, ρ, c, and κ are the material properties: density, heat capacity, and thermal conductivity, respectively. Ω represents the body domain of the problem, and $\partial_1\Omega$ and $\partial_2\Omega$ represent the surfaces of the problem with Dirichlet and Nuemann boundary conditions, respectively, with $\tilde{\boldsymbol{\theta}}$ as the prescribed temperature values, and $\mathbf{q}$ as the prescribed heat flux values. Finally, $\boldsymbol{\theta}_0$ are the given initial conditions for

*https://github.com/smdogroup/tacs

†https://github.com/OpenMDAO/OpenMDAO

‡https://github.com/OpenMDAO/dymos

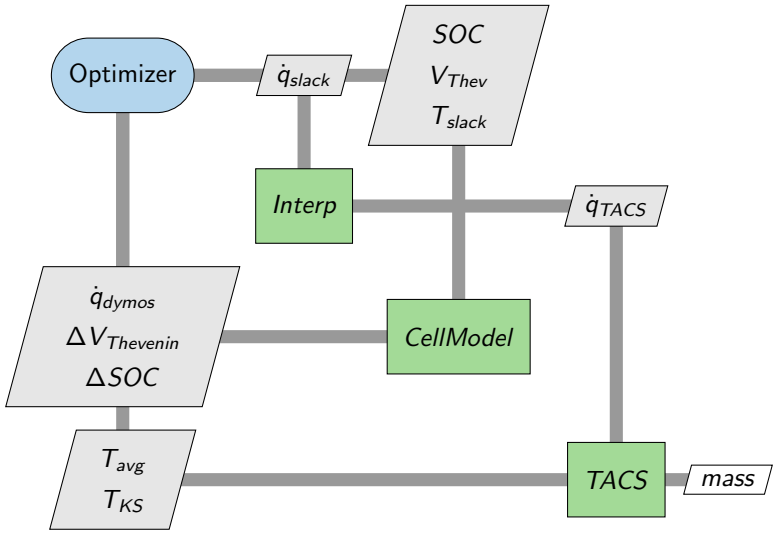

Fig. 2 eXtended Design Structure Matrix (XDSM) showing the coupling between the transient finite element heat transfer model ("TACS") and the cell-discharge battery model ("CellModel").

the problem. The heat boundary conditions of the problem, $\mathbf{q} = \mathbf{q}(t)$ are to be supplied by the cell-discharge model as a function of time. These are a function of how much power the optimizer selects from the electric propulsion system and therefore vary in time as well as during a trajectory optimization.

The continuous form of the heat-transfer equations in Eq. (1) are expressed in discrete form as:

$$\mathbf{C}\dot{\mathbf{u}}_k + \mathbf{H}\mathbf{u}_k = \mathbf{Q}_k, \;\; k = 1, \ldots, n \tag{2}$$

In this work, we use the Backwards Difference Formula (BDF) integration scheme to compute the time-dependent states with a Newton solver using residual equations in the form of:

$$\left[\frac{\alpha_0}{\Delta t}\frac{\partial \mathbf{R}}{\partial \dot{\mathbf{u}}} + \frac{\partial \mathbf{R}}{\partial \mathbf{u}}\right] \Delta \mathbf{u}_k = -\mathbf{R}\left(\dot{\mathbf{u}}_k, \mathbf{u}_k, \mathbf{x}, t_k\right), \;\; k = 1, \ldots, n \tag{3}$$

Throughout this work, we use the geometry and mesh for the battery pack shown below in Fig. 1, where the regions shaded in red indicate the battery cells, and the region shaded in gray indicate the battery case material. The geometry represents a 3×3 grid of cells enclosed in aluminum. This represents a major reduction in the actual numbers of cells that would be used, but this is an acceptable simplification due to the symmetry of the geometry and the uniformity of the heat flux boundary conditions. We also assume uniform temperature distribution in the out-of-plane dimension, so to further reduce computational cost, we use a 2D mesh with plane-stress elements and apply a uniform thickness of 65 mm. Each cell has a diameter of 18 mm, and the length and width at the widest points of the geometry is 62.19 mm. In Fig. 1, s represents the spacing distance between the cells, normalized by the cell diameter d_{cell}, r indicates the radius of holes in pack, and $r_{\max}$ indicates the maximum possible hole size. These shape parameters are discussed further in Section II.C. Aluminum is used as the case material, and the material properties of the batteries is representative of 18650-type cylindrical cells, with material properties of each given in Table 1.

Table 1 Material properties of each material used in the heat transfer model.

	Case	Cells
Density, ρ (kg/m^3)	2700	1460
Heat capacity, c (J/kg $\cdot$ K)	883	880
Thermal conductivity, κ (W/m $\cdot$ K)	204	1.3

Throughout the work presented in this paper, we apply a scalar, time-varying heat flux to each battery in the domain, represented as $\dot{q}(t_k),\ k = 1, \ldots, n$, with $t_{k=1} = 0$ and $t_{k=n} = t_f$, where t_f is the final time in the simulation. The initial conditions start with the pack at a uniform temperature of 25 °C, and there are no surfaces in the domain with a fixed temperature boundary condition of the form $\boldsymbol{\theta} = \tilde{\boldsymbol{\theta}}$, on $\partial_1\Omega$. We approximate ambient cooling of the pack by adding 5 W of cooling at each time-step to the case material.

The cell discharge model uses a time-varying scalar value of battery temperature as an input. This is computed in TACS by taking the spatial average temperature of all batteries as a function of time, represented as $\mathbf{T}_{\text{avg}} \in n_{\text{TACS}}$. For safety considerations, we are also interested in constraining the maximum battery temperatures to keep them below their operating limit. We do this by evaluating the approximate maximum temperature over all batteries using the Kreisselmeir-Steinhauser (KS) function [11]. This approximate maximum function is taken over all points in the domain as well as over all points in time, resulting in a single, scalar value, T_{KS}.

TACS includes the capability to compute derivatives of functions of interest using the adjoint method. To enable coupling with the cell-discharge model, we are interested in the derivative of the time-varying average temperature function, $\mathbf{T}_{\text{avg}}(t)$ with respect to the time-varying scalar heat flux, $\dot{\mathbf{q}}(t)$. We evaluate this derivative as:

$$\frac{\mathrm{d}\mathbf{f}}{\mathrm{d}\dot{\mathbf{q}}} = \frac{\mathrm{d}\mathbf{f}}{\mathrm{d}\mathbf{Q}}\frac{\mathrm{d}\mathbf{Q}}{\mathrm{d}\dot{\mathbf{q}}} = \boldsymbol{\psi}^T\frac{\mathrm{d}\mathbf{Q}}{\mathrm{d}\dot{\mathbf{q}}} \tag{4}$$

where $\mathbf{Q}$ is the right-hand-side vector of the linear system, $\boldsymbol{\psi}$ is the adjoint vector, and $\mathbf{f}$ represents the time-varying average temperature function. The right-hand-side vector $\mathbf{Q}$ is constructed as:

$$\mathbf{Q}_k = \dot{q}_k\mathbf{Q}_0 + \mathbf{Q}_{\text{cooling}} \tag{5}$$

where $\mathbf{Q}_0$ is a time-invariant right-hand-side vector that represents a unit heat-flux applied uniformly to each cell. Differentiating $\mathbf{Q}_k$ with respect to $\dot{q}_k$ simply results in $\mathbf{Q}_0$, which can be substituted back in to Eq. (4).

B. Battery Cell Discharge Model

The battery model is a cell-level model based on previous work by Chin et al. [4], which uses experimental cell discharge data to fit a Thevenin voltage open-circuit model to solve an ordinary differential equation (ODE) for state-of-charge (SOC) and Thevenin voltage as a function of cell temperature:

$$U_{\text{oc}}, C_{\text{Th}}, R_0, R_{\text{Th}} = f\left(SOC, T_{\text{batt}}\right) \tag{6}$$

where U_{oc} is the open-circuit voltage, C_{Th} is the Thevenin equivalent capacitance, R_0 is the Ohmic resistance, and R_{Th} is the polarization resistance. The cell-level parameters from Eq. (6) are computed using a basic linear interpolation provided in OpenMDAO. Further details of the cell-level model can be found in Chin et al. [4]. For the context of the optimization problems in this paper, we use a battery pack that has been previously sized for a TTBW aircraft [9], which uses 170 cells in series (n_{s}), and 40 cells in parallel (n_{p}). The model uses cell characteristics representative of an 18650 cell with 3000 mAh capacity and 15 Amp max discharge.

C. Mesh Deformation

When we include shape parameters as design variables in the optimization problem, we require a way to deform the finite-element mesh corresponding to changes in the shape parameters. For the geometry shown in Fig. 1, we use two shape parameters, ϕ and s, where $\phi = r/r_{\text{max}}$ controls the size of the holes in the pack, normalized by the maximum allowable hole size, and s controls the spacing between the cells, normalized by the diameter of the cell. The geometry and shape parameters are the same as were used in previous battery pack shape optimization work by Chin et al. [5]. Both shape parameters are defined in such a way that always produce feasible geometries, provided that $\phi \in [0, 1]$ and $s \in [1, \infty)$.

For shape parameters to be included in the optimization problem, mesh deformation is needed to update the finite element mesh. Mesh deformation provides a differentiable way of updating the finite-element mesh, whereas mesh re-seeding would produce discontinuities in the optimization problem. The mesh deformation component takes changes in the shape parameters, Δs and $\Delta\phi$ as inputs, and computes updated mesh node locations, $\mathbf{X}_{\text{node}}$, as the output. The updated mesh node locations are passed to the thermal analysis component as an input. The connectivity of the mesh remains constant during the update, so that only the node locations are updated. The XDSM for the optimization

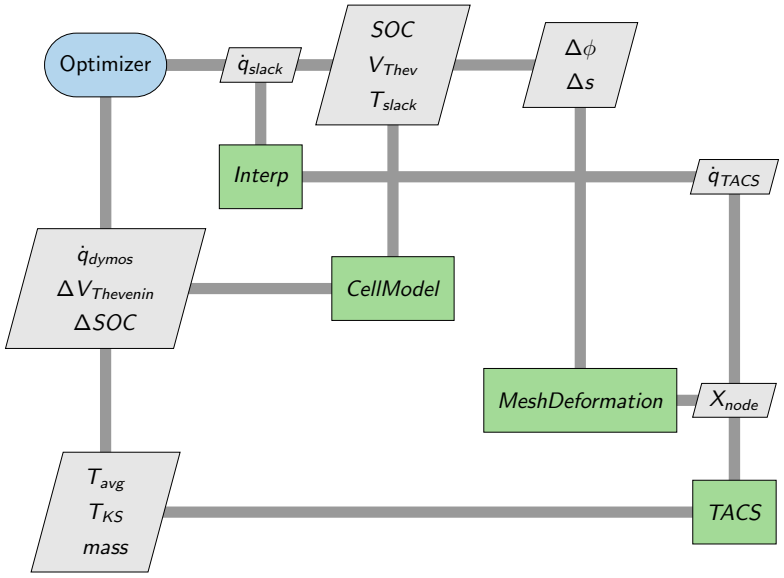

Fig. 3 eXtended Design Structure Matrix (XDSM) showing the coupling between the transient finite element heat transfer model ("TACS") and the cell-discharge battery model ("CellModel") with shape parameters included in the optimization problem.

problem including shape optimization is shown in Fig. 3, which illustrates the connection between the mesh deformation component and the thermal heat transfer analysis component.

The mesh deformation approach here is based on the work from Yildirim et al. [12]. The approach we use starts by identifying nodes on the boundary of the geometry. We refer to these nodes as "control nodes", and we can deform them directly by simply changing the shape parameter. That is, we can find an analytic form for the displacement of these nodes directly from their starting position and the shape parameters. Once we compute the displacement of the control nodes, the other nodes in the mesh (referred to as "dependent nodes") are computed as a function that is a weighted sum over all of the control nodes. The displacement of dependent node i is given as

$$\Delta\mathbf{x}_i = \frac{\sum_j^{n_c} \mathbf{w}_{ij}\Delta\mathbf{x}_j}{\sum_j^{n_c} \mathbf{w}_{ij}}, \tag{7}$$

where

$$\mathbf{w}_{ij} = \frac{1}{||\mathbf{x}_i - \mathbf{x}_j||_2^m}, \tag{8}$$

where $\Delta\mathbf{x}_i$ is the displacement of the i^{th} dependent node, $\Delta\mathbf{x}_i = (\Delta x_i, \Delta y_i)$ for 2D problems, n_c is the number of control nodes in the mesh, $\mathbf{w}_{ij}$ is the distance-weighting of dependent node i to control node j, and m is an exponent which is set equal to 2 in this work.

Figure 4 shows an example of this mesh deformation approach. Points are generated in a square with a hole in the middle; the hole radius is then increased from 0.25 to 0.35, and the deformation of the dependent nodes is computed. Control nodes are shown in red, and dependent nodes are shown in blue. Note that nodes along square border are included as control nodes even though this border remains constant. The displacement of these nodes is prescribed to be zero in order to keep the outer dimensions constant. This approach can be easily built-up to more complex cases where we can still easily prescribe the desired shape deformation.

Finally, we need to compute the derivatives of the node displacements with respect to the shape parameters. The control node displacement derivatives can be computed directly since they are analytic functions. Next, to compute the derivative of the dependent node displacements with respect to the shape parameters, in Eq. (7), simply replace $\Delta\mathbf{x}_j$ with the control node displacement derivatives. TACS can compute the derivatives of the function outputs ($\mathbf{T}_{\text{avg}}$, T_{KS}, and mass) with respect to the node locations, $\mathbf{X}_{\text{node}}$, using the adjoint method. These mesh-deformation derivatives are

multiplied by the derivatives of the functions with respect to node locations to compute compact total derivatives of the form:

$$\frac{\mathrm{d}f}{\mathrm{d}y} = \frac{\mathrm{d}f}{\mathrm{d}\mathbf{X}_{\text{node}}} \frac{\mathrm{d}\mathbf{X}_{\text{node}}}{\mathrm{d}y} \tag{9}$$

where f represents any of the function outputs computed by TACS ($\mathbf{T}_{\text{avg}}, T_{\text{KS}}$, or mass) and y represents either of the shape parameter updates (Δs or $\Delta\phi$).

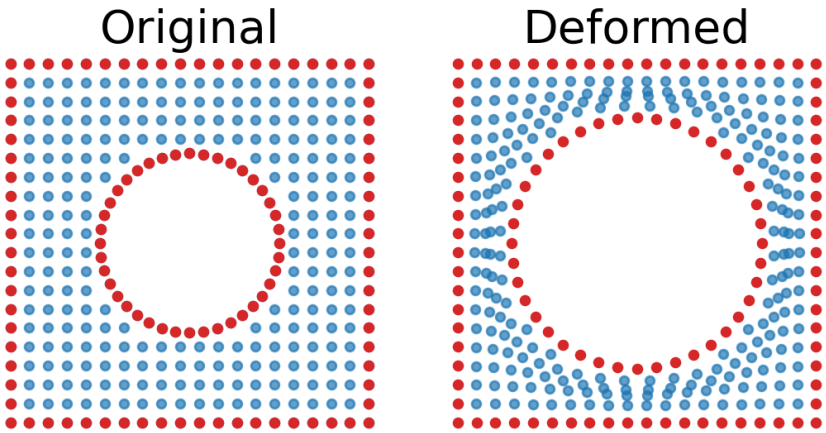

Fig. 4 Demonstration of mesh deformation approach, with original nodes on the left and the deformed nodes shown on the right. Control nodes are shown in red, and dependent nodes are shown in blue.

III. Results

In this section, we present results for two different optimization problems. The first set of results in Section III.A demonstrates the coupling between the cell discharge battery model and the transient finite element heat transfer model, using the model structure illustrated in Fig. 2. The next set of results in Section III.B adds shape optimization to the coupled optimization problem, using the model shown in Fig. 3.

A. Coupled Battery Pack Trajectory Optimization

Here we present optimization results which demonstrate coupling between the cell discharge battery model and the transient finite element heat transfer model. The problem formulation is defined to minimize the state-of-charge (SOC) of the battery pack without violating a maximum temperature constraint on the battery cells. The pack current is defined to be a control that the optimizer can optimize. Current directly affects the rate of change of SOC through the cell discharge model, which also directly affects the rate of heat generation of the battery pack, Q. The heat generation feeds into the heat transfer analysis of the battery pack, which determines the battery cell temperatures. This problem assumes a fixed duration for the analysis of 300 seconds, and the pack geometry remains constant as well. The results in this section use the problem formulation provided in Eq. (10), and the model structure shown in Fig. 2. The optimization convergence criteria is set to 10^{-3} for both optimality and feasibility. The minimum allowable current is 10 Amps, the maximum allowable current is 1,000 Amps, and the maximum battery temperature is 55 °C.

$$\begin{aligned}
\min \quad & \text{SOC}_{\text{final}} \\
\text{with respect to} \quad & I_{\text{min}} \leq \mathbf{I} \leq I_{\text{max}} \\
& \mathbf{T}_{\text{slack}} \\
& \mathbf{q}_{\text{slack}} \geq 0 \\
\text{such that} \quad & T_{\text{KS}} \leq T_{\text{max}} \\
& \mathbf{q}_{\text{slack}} = \mathbf{q}_{\text{dymos}} \\
& \mathbf{T}_{\text{slack}} = \mathbf{T}_{\text{avg}}
\end{aligned} \tag{10}$$

The results of the optimization are shown in Fig. 5, which provides time-histories of total pack current, pack heat generation, Q, average battery temperature, and state-of-charge. The current starts at the lower bound of 10 Amps and ramps up quickly to approximately 410 Amps, and it maintains this value for the majority of the duration. Close to the end of the simulation, the current ramps up quickly to 962 Amps, which is nearly the maximum allowable value. The total heat generated by the pack is shown in the next figure down, and intuitively, this follows a nearly identical trend as current. The reason for ramping up current rapidly at the end is that this prevents this heat from being propagated through the pack during the simulation, resulting in a slightly lower value of T_{KS}. This allows slightly more SOC to be extracted out of the pack without violating the temperature constraint. The average cell temperature is the next subfigure down, shown in yellow. This average cell temperature increases monotonically, but there are noticeable differences in the rate of change which correspond to higher or lower heat flux values. Also note that this is the time-varying average cell temperature, $\mathbf{T}_{\text{avg}}$, not the constraint value T_{KS}, which ends up at the expected upper limit of 55 °C. Finally, the bottom-most subfigure shows the time-history of SOC in red. This follows a monotonically decreasing trend, with noticeable rate changes corresponding to the current value. The temperature distribution within the battery pack at the final time-step is shown in Fig. 6, which shows the battery cells as being slightly warmer than the surrounding pack. This is due to their low thermal conductivity relative to the surrounding pack, which also leads to a noticeable temperature gradient within in the cells.

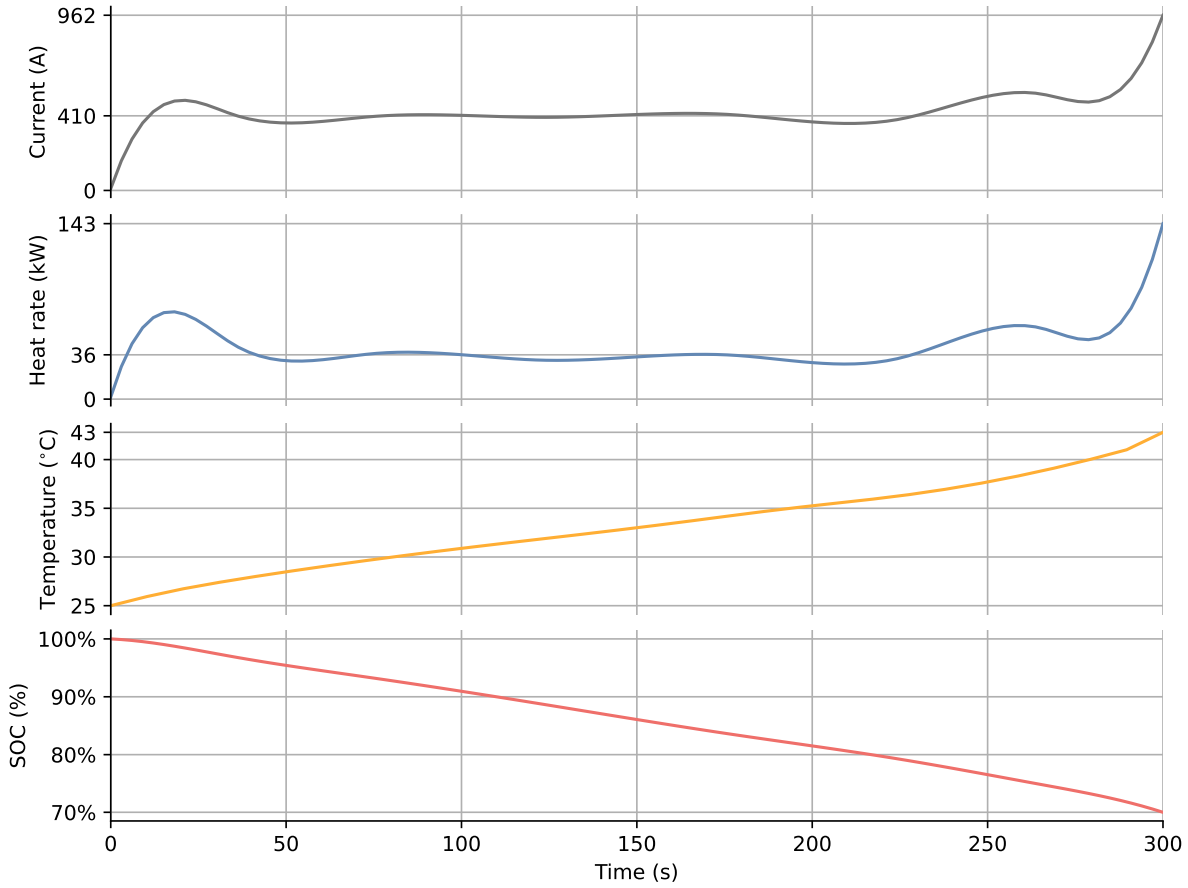

Fig. 5 Time-history of the battery pack optimization with coupled cell-discharge and transient finite element heat transfer for results in Section III.A. From top to bottom: total battery pack current (Amps), total battery pack heat generation (kilowatts), average temperature of the battery cells (Celsius), and battery pack state-of-charge (%).

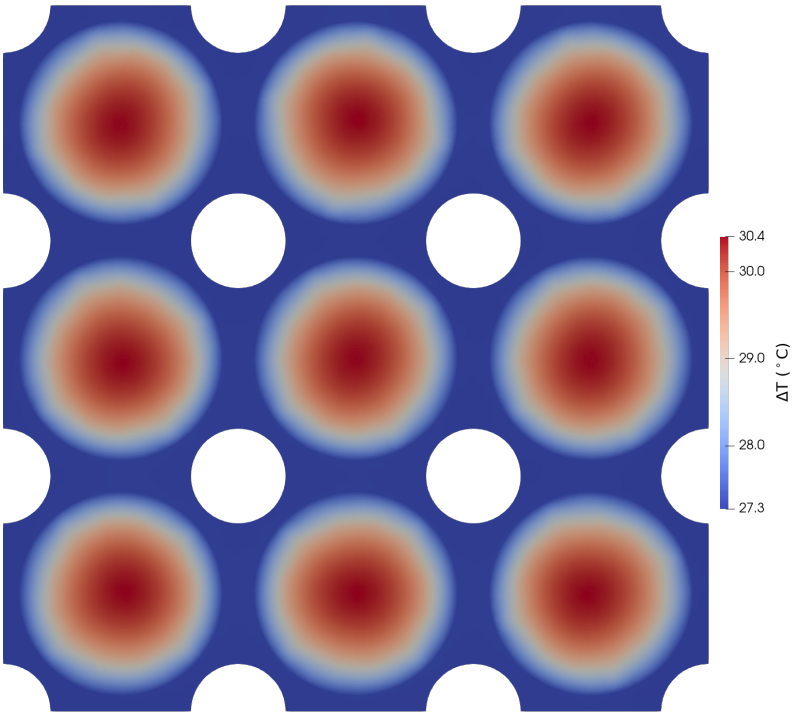

Fig. 6 Temperature distribution within the battery pack at the final time-step for results in Section III.A.

B. Simultaneous Trajectory and Shape Optimization

In this section, we build on the results from Section III.A by adding shape optimization of the battery pack to the optimization problem. Previously, the geometry was fixed, and therefore the battery pack mass was also fixed. By adding the shape parameters as design variables, we can now improve the energy density of the battery pack by allowing the optimizer to design a lighter-weight, yet feasible, pack. Given the fixed time duration of the analysis, it is still important to utilize the battery pack as much as possible while also considering the temperature constraints on the battery cells. To accommodate these dual objectives, we use a composite objective function in the form of:

$$f = \text{SOC}_{\text{final}} + \alpha \frac{m}{m_{\text{ref}}} \tag{11}$$

where m is the battery pack mass, and m_{ref} is a reference mass, which we set as the initial mass of the undeformed pack geometry. For this 9-cell configuration, the initial pack geometry is 0.408 kg. We leave $\text{SOC}_{\text{final}}$ unscaled because the values are bounded between 0.2 and 1. The parameter α is used to scale the relative importance of mass versus SOC in the objective function. For the results shown here, α is set to 1 so that both objectives are equally weighted. The optimization problem including shape optimization is given in Eq. (12). The results shown in this section use the model structure shown in Fig. 3. The shape parameter design variables, $\Delta\phi$ and Δs, are bounded by corresponding upper and lower bound values, denoted by the subscripts "ub" and "lb", respectively. The initial value of the spacing parameter s is 1.1516, with a lower bound of 1.1, and an upper bound of 2.0. The initial value of the hole-size parameter is 0.7381, with an upper bound of 0.85, and a lower bound of 0.4. The theoretical range of values for s is $[1, \infty)$, and for ϕ is $[0, 1]$; however, we restrict the values to be within a tighter range to preserve mesh quality.

$$
\begin{aligned}
\min \quad & f = \mathrm{SOC}_{\mathrm{final}} + \alpha \frac{m}{m_{\mathrm{ref}}} \\
\text{with respect to} \quad & I_{\min} \leq \mathbf{I} \leq I_{\max} \\
& \mathbf{T}_{\mathrm{slack}} \\
& \mathbf{q}_{\mathrm{slack}} \geq 0 \\
& \Delta\phi_{\mathrm{lb}} \leq \Delta\phi \leq \Delta\phi_{\mathrm{ub}} \\
& \Delta s_{\mathrm{lb}} \leq \Delta s \leq \Delta s_{\mathrm{ub}} \\
\text{such that} \quad & T_{\mathrm{KS}} \leq T_{\max} \\
& \mathbf{q}_{\mathrm{slack}} = \mathbf{q}_{\mathrm{dymos}} \\
& \mathbf{T}_{\mathrm{slack}} = \mathbf{T}_{\mathrm{avg}} \\
& \mathrm{SOC}_{\mathrm{final}} \geq 20\%
\end{aligned}
\tag{12}
$$

The results for the coupled shape optimization are shown in Fig. 7, including time-histories of total pack current, pack heat generation, average battery temperature, and state-of-charge. In this case, current ramps up quickly to over 1,000 Amps and then back down again quickly, and then remains near 200 Amps until the end of the simulation when it ramps up again to 1,000 Amps. While the initial overshoot appears to violate the maximum current of 1,000 Amps, the control points governing the spline interpolation never do, so the exceedance is not registered in the optimization as a constraint violation. Again, the pack heat generation follows a very similar trend as the current. The temperature shows a relatively fast ramp up to approximately 40 °C, but increases only slightly between 100 seconds and 300 seconds, when it reaches a final value of 43 °C. The KS-aggregated maximum temperature in this case again is exactly satisfied at 55 °C. The trend of SOC in this case appears much more nonlinear than the initial optimization result, with a steep initial drop, followed by the rate becoming more shallow and steadier. In this case, we see a larger final SOC value of 78% compared to the previous result without shape optimization which resulted in a final SOC of 70%. Discharging the battery pack less results in less heat rejected to the cells and pack, which allows the pack to become lighter.

The results from the two optimization problems are compared in Table 2, with results from the initial optimization (III.A) given in the "Baseline" column, and results including shape optimization given in the "Final" column. Values are given for pack mass, KS-aggregated maximum temperature (T_{KS}), shape parameters s and ϕ, and final SOC, along with the relative difference of each value from the baseline to the final design. Overall, the shape-optimization problem results in a 15% lighter pack, at the expense of 11% less SOC being discharged. Also note that both shape parameters end up at one of their bounds (spacing s is at its lower bound, and relative hole size ϕ is at its upper bound), which is the lightest-weight design allowable given the constraints. Figure 8 shows the initial and final pack geometries.

Table 2 Summary of shape optimization results and comparison against initial optimization results without shape optimization (baseline).

	Baseline	**Final**	**Difference**
Mass (kg)	0.408	0.345	15% ↓
T_{KS} (°C)	55	55	0
s	1.1516	1.1	4% ↓
ϕ	0.7381	0.85	15% ↑
$\mathrm{SOC}_{\mathrm{final}}$	70%	78%	11% ↑

IV. Conclusion

Battery performance is intricately connected to the thermal state of the battery cells; temperature is an input to the Thevenin-equivalent circuit discharge model, which computes battery heat generation as an output. Heat flux is an input to the heat transfer analysis of the battery pack, which is used to compute the temperature of the battery cells. In this work, we describe a battery model which captures this two-way coupling, combining a cell-discharge model with a transient finite-element heat transfer model. We demonstrate this coupled battery model through a trajectory optimization of the battery pack current, which is constrained by the maximum temperature of the battery cells. We

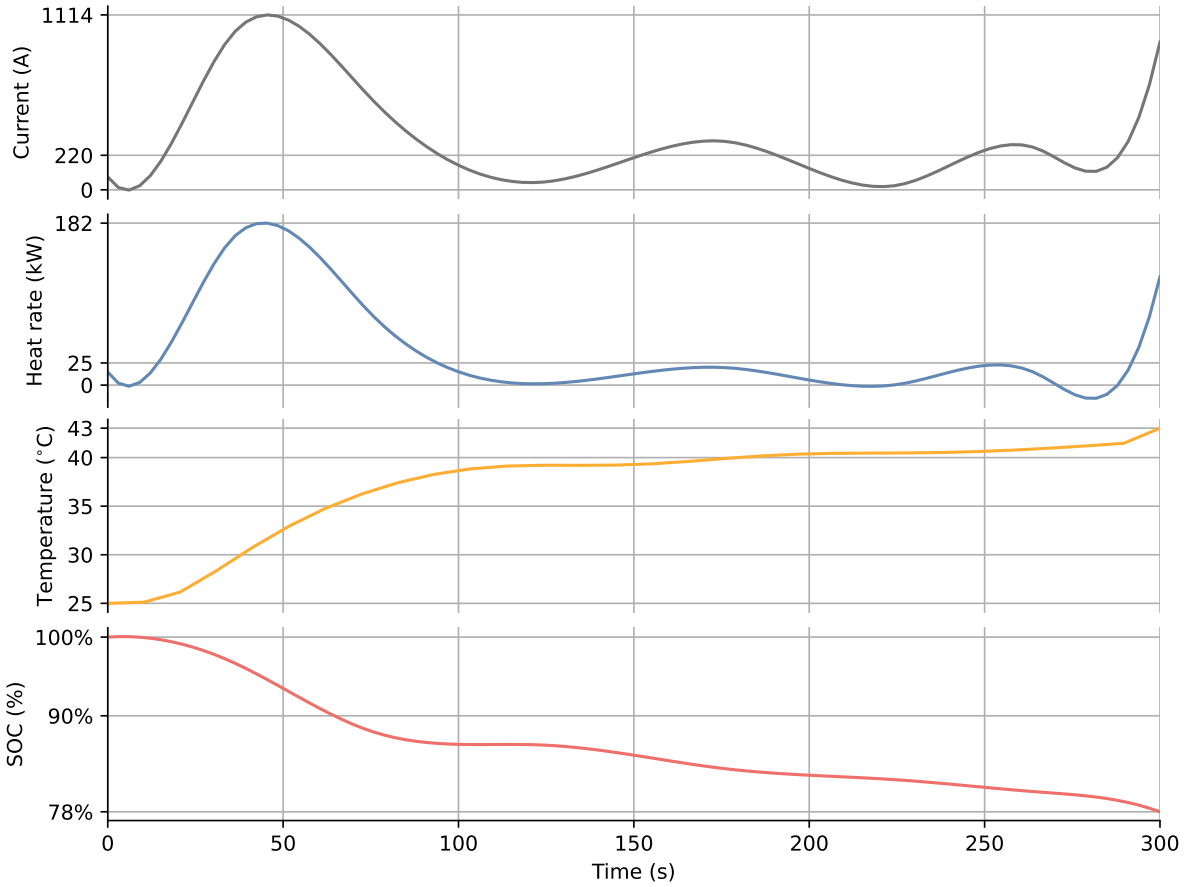

Fig. 7 Time-history of the battery pack optimization with coupled cell-discharge and transient finite element heat transfer and shape optimization for results in Section III.B. From top to bottom: total battery pack current (Amps), total battery pack heat generation (kilowatts), average temperature of the battery cells (Celsius), and battery pack state-of-charge (%).

also demonstrate the ability to generate light-weight battery pack designs by adding shape optimization to the coupled battery model, and performing a simultaneous trajectory and shape optimization of the battery pack using a composite objective function. Including this coupled battery model with shape optimization in an aircraft and mission optimization is a priority for future work so that the impact of the battery pack design can be better reflected in an aircraft and mission context.

Acknowledgments

The work presented in this paper was developed with support from NASA's Transformational Tools and Technologies (TTT) project. Funding for TTT is provided by the Aeronautic Research Mission Directorate (ARMD).

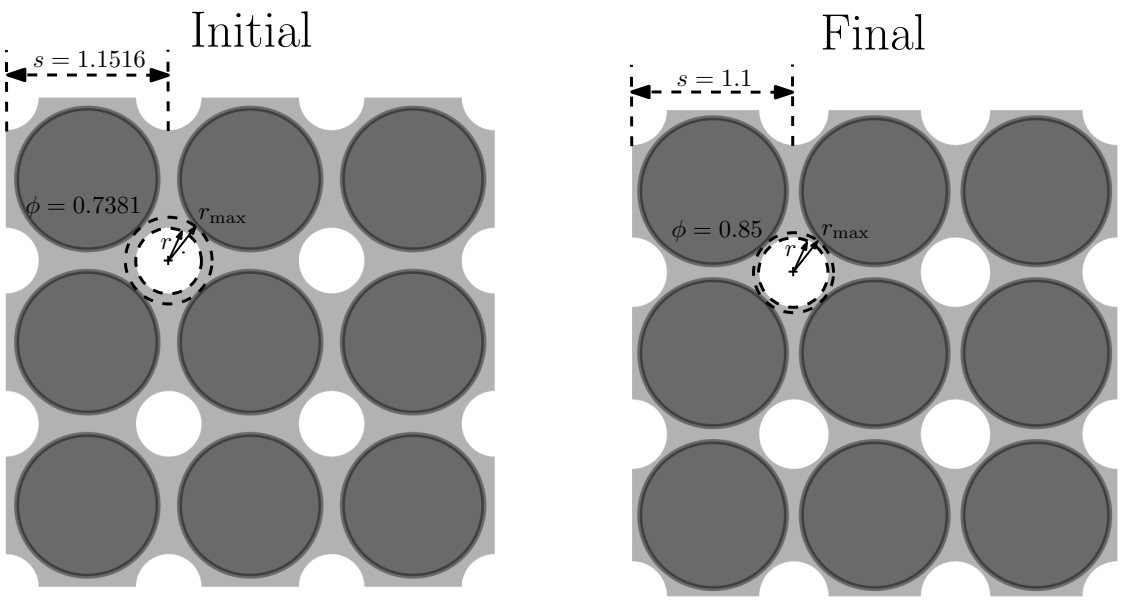

Fig. 8 Initial pack geometry (left), and final pack geometry (right) for the results presented in Section III.B. The initial design starts with a relative battery spacing of $s = 1.1516$, and a relative hole size of $\phi = 0.7381$. The final design results in a relative battery spacing of $s = 1.1$, and a relative hole size of $\phi = 0.85$.

References

[1] Quinlan, J., "Overview of Electrified Aircraft Propulsion at NASA," *Power and Energy Conference at Illinois*, 2024.

[2] Boopathy, K., and Kennedy, G. J., "Parallel finite element framework for rotorcraft multibody dynamics and discrete adjoint sensitivities," *AIAA Journal*, Vol. 57, No. 8, 2019, pp. 3159–3172.

[3] Kennedy, G. J., and Martins, J. R., "A parallel finite-element framework for large-scale gradient-based design optimization of high-performance structures," *Finite Elements in Analysis and Design*, Vol. 87, 2014, pp. 56–73.

[4] Chin, J., Schnulo, S. L., Miller, T., Prokopius, K., and Gray, J. S., "Battery performance modeling on SCEPTOR X-57 subject to thermal and transient considerations," *AIAA Scitech 2019 Forum*, San Diego, CA, 2019. doi:10.2514/6.2019-0784, AIAA 2019-0784.

[5] Chin, J. C., Look, K., McNichols, E. O., Hall, D. L., Gray, J. S., and Schnulo, S. L., "Battery Cell-to-Pack Scaling Trends for Electric Aircraft," *2021 AIAA/IEEE Electric Aircraft Technologies Symposium (EATS)*, Denver, CO, 2021. doi:10.23919/EATS52162.2021.9704819, AIAA-2021-3316.

[6] Gray, J. S., Hwang, J. T., Martins, J. R. R. A., Moore, K. T., and Naylor, B. A., "OpenMDAO: An open-source framework for multidisciplinary design, analysis, and optimization," *Structural and Multidisciplinary Optimization*, Vol. 59, No. 4, 2019, pp. 1075–1104. doi:10.1007/s00158-019-02211-z.

[7] Falck, R., Gray, J. S., Ponnapalli, K., and Wright, T., "dymos: A Python package for optimal control of multidisciplinary systems," *Journal of Open Source Software*, Vol. 6, No. 59, 2021, p. 2809. doi:10.21105/joss.02809.

[8] Aretskin-Hariton, E., Gratz, J., Kirk, J., Lyons, K., Jasa, J., Moore, K., Falck, R., Caldwell, D., Kuhnle, C., Recine, C., et al., "Multidisciplinary Optimization of a Transonic Truss-Braced Wing Aircraft using the Aviary Framework," *AIAA SCITECH 2024 Forum*, 2024, p. 1084. doi:10.2514/6.2024-1084, AIAA 2024-1084.

[9] Leader, M. K., Aretskin-Hariton, E., and Moore, K., "Multidisciplinary Optimization of a Transonic Truss Braced Wing Aircraft with Hybrid-Electric Propulsion," *AIAA Aviation 2024 Forum*, Las Vegas, NV, 2024. doi:10.2514/6.2024-4294, AIAA 2024-4294.

[10] Lambe, A. B., and Martins, J. R., "Extensions to the design structure matrix for the description of multidisciplinary design, analysis, and optimization processes," *Structural and Multidisciplinary Optimization*, Vol. 46, 2012, pp. 273–284. doi:10.1007/s00158-012-0763-y.

[11] Kennedy, G. J., and Hicken, J. E., "Improved constraint-aggregation methods," *Computer Methods in Applied Mechanics and Engineering*, Vol. 289, 2015, pp. 332–354. doi:10.1016/j.cma.2015.02.017.

[12] Yildirim, A., Mader, C. A., and Martins, J. R., "A surface mesh deformation method near component intersections for high-fidelity design optimization," *Engineering with Computers*, Vol. 38, No. 2, 2022, pp. 1393–1425. doi:10.1007/s00366-020-01247-w.